The transition to aeration in two-phase mixing in stirred vessels

Lyes Kahouadji, Fuyue Liang, Juan Valdes, Seungwon Shin, Jalel Chergui, Damir Juric, Richard Craster, Omar Matar

The transition to aeration in two-phase mixing in stirred vessels

Lyes Kahouadji[a], Assen Batchvarov[a], Cristian R. Constante Amores[a], Seungwon Shin[b], Jalel Chergui[c], Damir Juric[c], Richard V. Craster[d] and Omar K. Matar[a]

[a]Department of Chemical Engineering, Imperial College London, South Kensington Campus, London SW7 2AZ, United Kingdom

[b]Department of Mechanical and System Design Engineering, Hongik University, Seoul 121-791, Republic of Korea

[c]Laboratoire d'Informatique pour la Mécanique et les Sciences de l'Ingénieur (LIMSI), Centre National de la Recherche Scientique (CNRS), Université Paris Saclay, Bât. 507, Rue du Belvédère, Campus Universitaire, 91405 Orsay, France

[d]Department of Mathematics, Imperial College London, South Kensington Campus, London SW7 2AZ, United Kingdom

ARTICLE INFO

Keywords:
Stirred vessel
Mixing
Aeration
Front-tracking
CFD
Fluid Structure Interaction

ABSTRACT

We consider the mixing of a viscous fluid by the rotation of a pitched blade turbine inside an open, cylindrical tank, with air as the lighter fluid above. To examine the flow and interfacial dynamics, we utilise a highly-parallelised implementation of a hybrid front-tracking/level-set method that employs a domain-decomposition parallelisation strategy. Our numerical technique is designed to capture faithfully complex interfacial deformation, and changes of topology, including interface rupture and dispersed phase coalescence. As shown via transient, three-dimensional direct numerical simulations, the impeller induces the formation of primary vortices that arise in many idealised rotating flows as well as several secondary vortical structures resembling Kelvin-Helmholtz, vortex breakdown, blade tip vortices, and end-wall corner vortices. As the rotation rate increases, a transition to 'aeration' is observed when the interface reaches the rotating blades leading to the entrainment of air bubbles into the viscous fluid and the creation of a bubbly, rotating, free surface flow. The mechanisms underlying the aeration transition are probed as are the routes leading to it, which are shown to exhibit a strong dependence on flow history.

1. Introduction

Flow mixing inside a stirred vessel occurs in a large array of industrial applications and produces complex dynamical structures. These structures, such as those seen in the work of Batels et al. (2002) for single-phase flow, exert a strong influence on the mixing efficiency. Many fast-moving consumer goods involve the manufacturing of so-called structured products (e.g., foods, creams, detergents), which, in turn, result from the multiphase mixing of several types of base products in an open stirred vessel similar to the one shown schematically in Fig. 1. Some viscous products require rapid mixing but in the absence of bubble creation that lead to undesirable partial bottle-filling and process inefficiencies. In contrast, for other processes, such as those that deploy bioreactors, for instance, the promotion of 'aeration' is essential. Thus it is crucial to predict the mixing patterns in stirred vessels, and to demarcate the aeration threshold as a function of the relevant system parameters, such as fluid properties, and impeller geometry and rotational speed.

Given the broad range of applications, there have been numerous studies within the fluid mechanics mixing which have focused on flow sandwiched between a rotating disk at the base of a cylinder and a free surface. These studies have covered steady and unsteady, axisymmetric and three-dimensional, and flat as well as deoformable free surface flows. The visualisations of Spohn (1991) demonstrated development of an intriguing variety of secondary toroidal structures, which form even under steady, laminar, and axisymmetric conditions. Spohn (1991) and Spohn et al. (1993, 1998) reported that the secondary circulation was not always located along the rotating axis, as for an enclosed cavity, but could also be attached to the interface. Daube (1991) performed the first axisymmetric direct numerical simulation assuming a flat, stress-free, free surface, which was later extended by Lopez (1995).

The deformation of the free surface created by the rotating disk was explored experimentally by Vatistas (1990). The interface shape initially forms an inverted bell, and as the rotation rate increases, the free surface descends to the rotating disk producing a dry region on the disk in the form of a periodic pattern in the azimuthal direction. Experiments for flows creating sloshing (Vatistas et al., 1992) have provided a flow pattern map that highlights the most unstable azimuthal modes as a function of the fluid height at rest as a function of the disk angular velocity.

The experimental work of Suzuki et al. (2006) and Jansson et al. (2006) studied the variation of the height of the free surface at the axis of symmetry as a function of the Reynolds number (defined using the disk rotational speed and diameter). Four states are described by increasing the Reynolds number: an axisymmetric and steady-state where the interface resembles an inverted bell; a switching state where the interface reaches the rotating disk and dries it from its centre; an asymmetric state with the interface assuming the shape of two rotating concave surfaces; and a state in which the interface regains its symmetrical shape forming a single axisymmetric concavity. Jansson et al. (2006) provided a flow regime map that highlights the unstable azimuthal mode as a function of the disk speed and the flow aspect ratio (fluid height/tank radius). Piva and Meiburg (2005) proposed a first numerical approximation to detect the free surface de-

thumbnails/email.jpeg
l.kahouadji@imperial.ac.uk (L. Kahouadji)
ORCID(s): 0000-0001-8805-1192 (L. Kahouadji)

flection but this is limited to small deformations. Kahouadji and Martin Witkowski (2014) performed a numerical study that takes into account the axisymmetric interfacial deformation using curvilinear coordinates.

In all of the work reviewed in the forgoing, the motion is driven by a rotating disk rather than an impeller with far fewer studies focusing on the detailed fluid dynamics associated with the latter. With the added complexity of a bladed impeller, we expect to see flow regimes reminiscent of this complex behaviour. Ciofalo et al. (1996) performed a three-dimensional turbulent flow simulation, where the flow equations are in the rotating reference frame of the impeller with the addition of a conventional linear logarithmic "wall function" as in Launder and Spalding (1974). Brucato et al. (1998) compared alternative computational methods: the first replaced the impeller by suitable boundary conditions, and the second consisted of dividing the computational domain into two concentric and partially-overlapping parts; the inner region, containing the impeller, where the flow is simulated in a rotating reference frame of the latter, while in the outer region, simulations are conducted in the laboratory reference frame. This technique requires information exchange between the two regions. More recently, Li et al. (2017) coupled a volume-of-fluid method with a Reynolds stress model in order to capture the gas-liquid interface and the turbulent flow agitated by pitched blade turbines where the interface deflection reached the impeller hub.

To the best of our knowledge, studies involving direct numerical simulation of unsteady, deformable free surface flows have been restricted to situations wherein the interface deflection does not descend beyond the impeller blades. As a result, these studies are unable to analyse, in detail, the rich and complex vortical structures accompanying such flows. Furthermore, the phenomenon of aeration has not yet been studied in detail via numerical simulations, despite its obvious importance to industrial applications as highlighted above. Aeration involves the development of sufficiently large interfacial deformations that lead to the interaction of the free surface with the rotating impeller. This, in turn, brings about the entrainment and dispersion of the lighter phase into the underlying denser phase; for gas (air)-liquid systems, the dispersed phase corresponds to bubbles (of air). Our aim in the present paper is to study the intricacies of the two-phase mixing flows in a stirred vessel via three-dimensional direct numerical simulations by coupling Direct-Forcing Methods for the impeller Fadlun et al. (2000); Mohd-Yusof (1997) with a front-tracking technique for the interface Shin et al. (2017, 2018). Our results will elucidate the transition to aeration and its dependence on flow history (e.g., ramping up impulsively from from a stationary state vs increasing the impeller rotational speed following the achievement of a steady-state at lower speeds).

The rest of this article is organised as follows. Sec.2 describes the configuration, sets out the governing equations, and summarises the computational methods. Section 3 presents results for both laminar and turbulent regimes highlighting the vortical structures occurring in such flows; the mechanisms leading to aeration are described, followed by a discussion of the turbulent aeration regime. Finally, concluding remarks are provided, and ideas for future work are outlined.

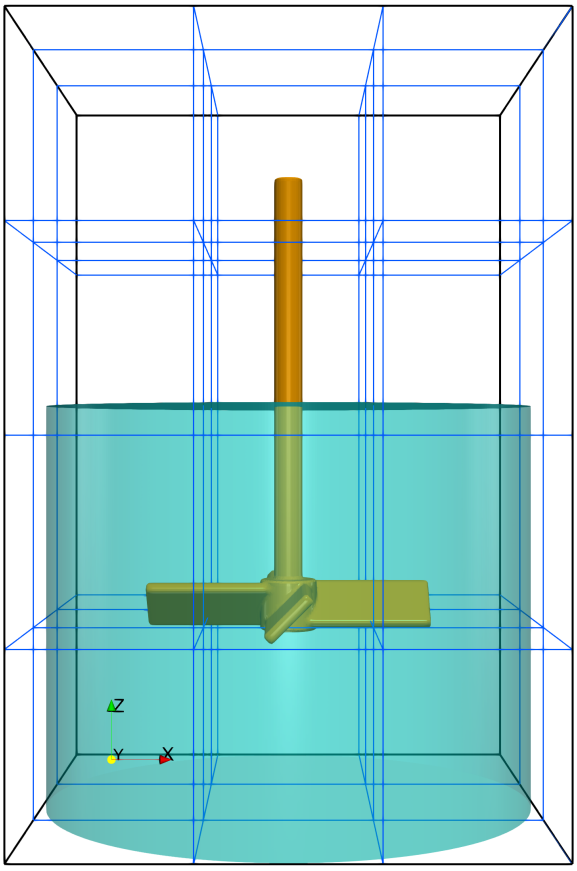

Figure 1: Schematic illustration of the computational domain: a stirred vessel configuration defined by an open cylindrical container, partially-filled with a viscous liquid, with a pitched-blade turbine immersed within it. The domain which is of size $8.6\times8.6\times13$ cm^3, and is divided into $3\times3\times4$ subdomains. The Cartesian structured grid per subdomain is 64^3, which gives a global structured mesh grid of $192\times192\times256$.

2. Problem formulation

The configuration we consider is shown in Fig. 1 and consists of a cylindrical vessel of diameter $D_b = 8.5$ cm filled with a viscous fluid up to a height $h = 7$ cm. The fluid is taken to be water or glycerine with air above in all simulations. The impeller consists of a cylindrical shaft of 0.5 cm diameter, a cylindrical hub of 1 cm diameter and 0.9 cm height, and four blades of 2.5 cm length, 1 cm height, 0.2 cm width, and inclined at $\alpha = 45^o$. The impeller is immersed inside the vessel with clearance $C = 3.5$ cm from the bottom of the vessel, and rotating at frequency f. The impeller diameter is $D_i = 5$ cm giving a ratio of radii between the vessel and the impeller $D_b/D_i = 1.7$. The characteristic length, velocity, and pressure scales are the impeller diameter, D_i, blade tip speed, $\pi f D_i$, and $\rho\left(\pi f D_i\right)^2$, respectively

that determine the Reynolds, Froude, and Weber numbers given by:

$$Re = \frac{\rho_l \pi f {D_i}^2}{\mu_l}, \quad Fr = \frac{\pi^2 f^2 D_i}{g}, \quad We = \frac{\rho_l \pi^2 f^2 {D_i}^3}{\sigma}. \tag{1}$$

We solve the Navier-Stokes equations, assuming incompressible and immiscible viscous fluids in a three-dimensional Cartesian domain $\mathbf{x} = (x, y, z) \in [0, 8.6]^2 \times [0, 13]$ cm:

$$\nabla \cdot \mathbf{u} = 0,$$
$$\rho \left(\frac{\partial \mathbf{u}}{\partial t} + \mathbf{u} \cdot \nabla \mathbf{u} \right) = -\nabla p + \nabla \cdot \mu \left(\nabla \mathbf{u} + \nabla \mathbf{u}^T \right) + \rho \mathbf{g} + \mathbf{F} + \mathbf{F_{fsi}}. \tag{2}$$

In Eqs. 2, $\mathbf{u}$ is the fluid velocity, t the time, p, the pressure, $\mathbf{g}$ the gravitational acceleration, $\mathbf{F}$, the local surface tension force, and $\mathbf{F_{fsi}}$ is the solid-fluid interaction force. We define $\mathbf{F}$ using a hybrid formulation (Shin et al., 2017, 2018):

$$\mathbf{F} = \sigma \kappa_{_H} \nabla I, \tag{3}$$

where σ, the surface tension coefficient, is assumed constant, and ϕ is an indicator function, equal to zero/unity for the gas/liquid phases. Numerically, this sharp transition is resolved across 3 to 4 grid cells with a steep, but smooth, numerical Heaviside function generated using a vector distance function computed directly from the tracked interface (Shin, 2007; Shin and Juric, 2009). In Eq. (3), $\kappa_{_H}$ is twice the mean interface curvature field calculated on an Eulerian grid using:

$$\kappa_{_H} = \frac{\mathbf{F}_{_L} \cdot \mathbf{G}}{\sigma \mathbf{G} \cdot \mathbf{G}}, \tag{4}$$

in which $\mathbf{F}_{_L}$ and $\mathbf{G}$ are respectively given by:

$$\begin{aligned} \mathbf{F}_{_L} &= \int_{\Gamma(t)} \sigma \kappa_{_f} \mathbf{n}_{_f} \delta_{_f} \left(\mathbf{x} - \mathbf{x}_{_f} \right) \mathrm{d}s \\ \mathbf{G} &= \int_{\Gamma(t)} \mathbf{n}_{_f} \delta_{_f} \left(\mathbf{x} - \mathbf{x}_{_f} \right) \mathrm{d}s. \end{aligned} \tag{5}$$

In these formulae, $\mathbf{x}_{_f}$ is a parameterisation of the interface, $\Gamma(t)$, and $\delta_{_f}(\mathbf{x} - \mathbf{x}_{_f})$ is a Dirac distribution that is non-zero only when $\mathbf{x} = \mathbf{x}_{_f}$, $\mathbf{n}_{_f}$ is the unit normal vector to the interface, and $\mathrm{d}s$ is the length of the interface element; $\kappa_{_f}$ is twice the mean interface curvature, but obtained from the Lagrangian interface structure. The geometric information corresponding to the unit normal, $\mathbf{n}_{_f}$, and length of the interface element, $\mathrm{d}s$, in $\mathbf{G}$ are computed directly from the Lagrangian interface and then distributed onto an Eulerian grid using the discrete delta function. The details follow Peskin's (Peskin, 1977) well-known immersed boundary approach using our procedure for calculating the force and constructing the function field $\mathbf{G}$.

The Lagrangian interface is advected by integrating

$$\frac{\mathrm{d}\mathbf{x}_{_f}}{\mathrm{dt}} = \mathbf{V}, \tag{6}$$

with a second-order Runge-Kutta method where the interface velocity, $\mathbf{V}$, is interpolated from the Eulerian velocity. Incorporating the complex geometry of the impeller and its rotation requires the implementation of the so-called Direct Forcing Method (Mohd-Yusof, 1997; Fadlun et al., 2000), which is done by incorporating a fluid-solid interaction force $\mathbf{F_{fsi}}$ in Eq. (2). This force is defined numerically using the latest step of the temporal integration of (2),

$$\rho \frac{\mathbf{u}^{n+1} - \mathbf{u}^n}{\Delta t} = \mathrm{local}^n + \mathbf{F}^n_{\mathbf{fsi}}, \tag{7}$$

where "local" stands for the right-hand-side terms of Eq. (2) that contain the convective, pressure gradient, viscous, gravitational, and surface tension force terms. Here, the superscripts denote the discrete temporal step in the computation.

In the solid part of the domain corresponding to the impeller, $\mathbf{F}^n_{\mathbf{fsi}}$ the forced rotational motion $\mathbf{V}^{n+1}$ is enforced:

$$\mathbf{u}^{n+1} = \mathbf{V}^{n+1} = 2\pi f \left(\left(y - y_0 \right), - \left(x - x_0 \right) \right), \tag{8}$$

where $(x_{_0}, y_{_0}) = (4.3, 4, 3)$ cm are the position of the impeller axis. Hence $\mathbf{F_{fsi}}$ is

$$\mathbf{F}^n_{\mathbf{fsi}} = \rho \frac{\mathbf{V}^{n+1} - \mathbf{u}^n}{\Delta t} - \mathrm{local}^n. \tag{9}$$

The no-slip condition is applied for the velocity and the interface at the edge of the impeller parts except for the shaft where we impose a solid rotating motion and axial free-slip condition $\partial \mathbf{u} / \partial z = 0$. Otherwise the interface will remain attached to the shaft.

The computational domain (see Fig. 1) is a rectangular parallelepiped where the entire domain is discretized by a uniform fixed three-dimensional finite-difference mesh and has a standard staggered MAC cell arrangement (Harlow and Welch, 1965). The velocity components u, v, and w are defined on the corresponding cell faces while the scalar variables (pressure p, and the distance function ϕ) are located at the cell centers. All spatial derivatives are approximated by standard second-order centred differences. The velocity field is solved by a parallel generalized minimal residual (GMRES) method (Saad, 2003) and the pressure field by a modified parallel 3D Vcycle multigrid solver based on the work of Kwak and Lee (2004) and described in Shin et al. (2017). Parallelisation is achieved using domain-decomposition where communication across processes is handled by Message Passing Interface (MPI) protocols.

The chosen pitched-blade turbine shown in Fig. 1 and described in the beginning of this section is built using a combination of primitive geometric objects (planes, cylinders, and rectangular blocks) where each object is defined by a static distance function $\psi(x, y, z)$, positive in the fluid and negative in the solid. The resulting shape in Fig. 1-(c) corresponds to the iso-value $\psi(x, y, z) = 0$. Details on how to construct similar complex objects are described in Kahouadji et al. (2018).

For Eqs. (2), (7), and (9), we use the single-field formulation for the density ρ and viscosity μ:

$$\begin{aligned} \rho(\mathbf{x}, t) &= \rho_g + \left(\rho_l - \rho_g \right) \phi(\mathbf{x}, t) \\ \mu(\mathbf{x}, t) &= \mu_g + \left(\mu_l - \mu_g \right) \phi(\mathbf{x}, t) \end{aligned} \tag{10}$$

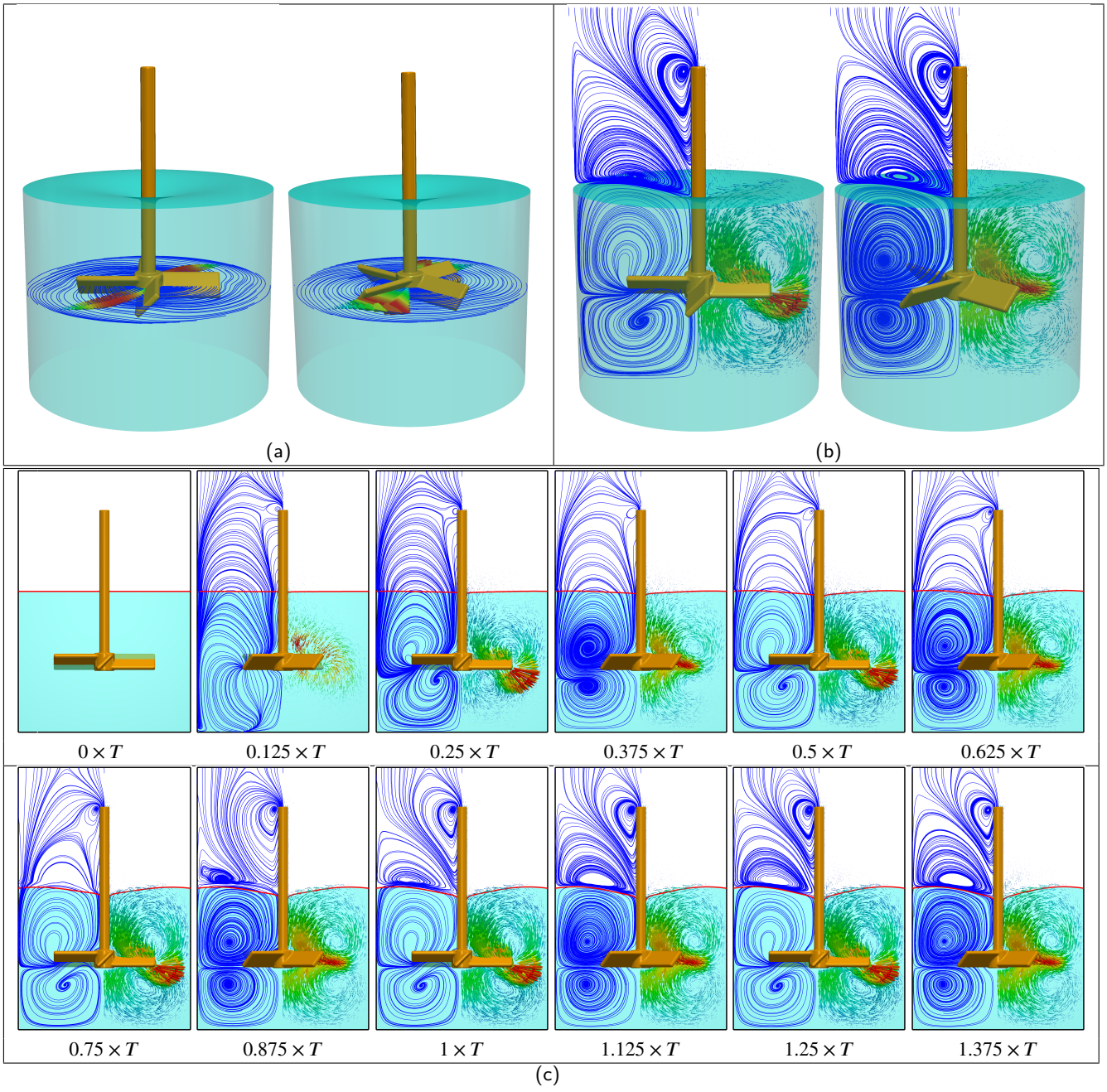

Figure 2: Laminar mixing flow for the case of glycerine with a rotational frequency $f = 1/T = 8$ Hz. The corresponding dimensionless numbers are $Re \sim 56$, $Fr \sim 3.22$, and $We \sim 1.55 \times 10^3$. Flow visualisation of the streamlines in the horizontal plane located at $z = 3.95$ cm, (a), and vertical plane $y = 0$, (b). Panel (c) shows snapshots of the streamlines in the $y = 0$ plane that illustrate the temporal evolution of the flow starting from rest (see Supplementary Material "Animation-Fig2.avi").

where the subscripts g and l designate the gas and liquid phases, respectively. The gas phase is considered as air, with constant physical properties at 20 °C ($\rho_g = 1.205$ kg/m^3 and $\mu_g = 1.825 \times 10^{-5}$ Pa.s). The liquid phase corresponds to either water or glycerine with the following properties: $\rho_l = 1000$ kg/m^3, $\mu_l = 10^{-3}$ Pa.s, and $\sigma = 0.0725$ N/m or $\rho_l = 1261.08$ kg/m^3 and $\mu_l = 1.4$ Pa.s, and $\sigma = 0.064$ N/m, respectively. Simulations with glycerine and water allow us to compare the two-phase mixing phenomena associated with laminar and turbulent flow regimes, respectively.

3. Results and discussions

We begin by describing the flow associated with the case of glycerine (Sec. 3.1) wherein the interface is slightly deformed. In section 3.2, we change the liquid from glycerine to water and highlight the emergence of complex vortical structures and a highly deformed surface; a large range of rotating frequencies, from $f = 5$ Hz to 9.5 Hz, is covered. The mechanisms leading to aeration are studied in Sec. 3.3 by close examination of the transition boundary between the

separated and dispersed flows. Finally, Sec. 3.4 focuses on the situation wherein air is entrained into the water across a highly deformed interface leading to bubbly mixing.

3.1. Laminar vortex mixing

The typical flow in the laminar regime is summarised in Fig. 2. Here, glycerine is chosen as the liquid phase and the rotation frequency is restricted to $f = 1/T = 8$ Hz so that the flow regime remains laminar, and the free surface deformation small, characterised by the following values of the relevant dimensionless numbers: $Re \sim 56$, $Fr \sim 3.22$, and $We \sim 1.55 \times 10^3$. The free surface deformation is defined as 'small' provided the amplitude of the deflection to the horizontal, divided by the characteristic length scale D_i, does not exceed 10%.

When the impeller blades are in motion, a centrifugal force is generated in the vicinity of the blades making the glycerine solution spiral out toward the tank periphery (see Fig. 2-(a)). This spiral motion reaches the fixed vessel wall, inducing the formation of two Stewartson boundary layers (Kahouadji and Martin Witkowski, 2014; Poncet, 2005; Stewartson, 1953) (at the top and bottom peripheries). The fluid motion reaches the free surface (bottom of the tank), it then decelerates by a centripetal spiral motion toward the rotating shaft (rotation axis) above (below) the impeller; this is analogous to the behaviour reported previously in the literature for the rotating disks (Daube, 1991; Spohn, 1991; Spohn et al., 1993, 1998; Piva and Meiburg, 2005; Kahouadji and Martin Witkowski, 2014). The flow is not axisymmetric, and one can see in Fig. 2-(a) and (b) that the position of the rotating blades matter in terms of understanding the reasons underlying the flow patterns (see Supplementary Material "Animation-Fig2.avi"). Under the pumping effect generated by the rotating blades, the fluid returns toward the rotating hub and blades by an upward swirling motion around the z-axis from the bottom, and by a downward swirling motion around the rotating shaft (see Fig. 2-(a) and (b)).

The temporal evolution, from a static initial condition $t = 0 \times T$ up to $t = 1.375 \times T$, is shown in Fig. 2-(c), which depicts the streamlines in the horizontal plane immediately below the hub, as well as in the $y = 0$ plane. From this figure, we can see that the free surface shape becomes essentially steady for $t > T$. This has similarity with the work of Kahouadji and Martin Witkowski (2014) who studied the free surface rotating flow generated by a rotating disk located at the bottom of a fixed cylindrical tank by solving the steady and axisymmetric Navier-Stokes equations using a vorticity-streamfunction formulation. Assuming a developed steady state, Kahouadji and Martin Witkowski (2014) considered the interface as a streamline. In the present case, as shown in Fig. 2(c), the streamlines cross the interface for $t < T$ indicating there is motion of the interface, whereas, for $t > T$, the interface becomes a streamline, and remains steady. It is also noteworthy that although the interface shape is steady and axisymmetric for $t > T$, the liquid flow is periodic in its azimuthal direction with a periodicity mode of 4, reflecting the fact that the impeller comprises four blades. Finally, we draw attention to the time required to make the entire flow quasi-steady: $t \sim T = 1/f = 1/8$ (s); this is in contrast to the cases which will be discussed below where, typically, 10 or $20 \times T$ are required to reach a quasi-steady state.

3.2. Turbulent vortex mixing

We replace the highly viscous glycerine with water and keep the frequency at $f = 8$ Hz so that the flow is characterised by $Re = 6.28 \times 10^4$, $Fr = 3.22$, and $We = 1.08 \times 10^3$, which indicates that it is expected to be turbulent, and accompanied by large interfacial deformations. We show in Fig. 3 the spatio-temporal behaviour of the flow for $f = 1/T = 8$ Hz from a static initial state until reaching a steady state for $t = 20 \times T$. It is seen that the free surface shape remains quasi-flat until the impeller has rotated 1.5 cycles (see Fig. 3-(a-e)). However, even though the interface is flat, the velocity magnitude on the interface Fig. 3-(d-j) shows that the velocity disturbance experiences a periodic distribution along its azimuthal direction with a wave number equal to 4, a symmetry that reflect the 4-blades of the impeller. At $t = 2 \times T$, the interface starts to deform (see Fig. 3-(f-l)), where the velocity gradient is high, leading to a periodic azimuthal interface deflection with wave number again 4 due to symmetry. The interface continues to undergo spatio-temporal variations until reaching a quasi-steady, and approximately axisymmetric state from $t = 10 \times T$, as shown in Fig. 3-(j-l), which is characterised by a maximal interfacial deflection.

The evolution of the vortical structures in the vertical plane shows the existence of very rich dynamics, as depicted in Fig. 3. At early times ($t \sim 0.25 \times T$), the impeller blades generate a large primary vortex that starts at the blade tips toward the bottom of the vessel and then moves upward near the vessel wall toward the interface. A secondary vortex is also generated under the impeller blades, which rotates radially in the opposite direction compared to the the primary vortex. This secondary vortex is generated from the bottom of the impeller hub and grows until reaching a situation of a two dipole-vortex, one above the impeller blades and the second below it (see the streamlines in Fig. 3-(c) and (d) for $t = 0.5$ and $1 \times T$).

At $t = 1.5 \times T$, the bottom vortex dissipates and we notice the creation of Kelvin-Helmholtz vortices that merge (at $t = 2 \times T$) into a single vortex below the impeller blades (see the streamlines in Fig. 3-(e,f)). These Kelvin-Helmholtz vortices are generated due to the fact that the primary top vortex rotates faster (due to the presence of the interface) than the secondary bottom vortex (due to the no-slip condition at the bottom of the vessel), and creates a large shear zone between these two vortices. For $t \geq 2 \times T$, the Kelvin-Helmholtz vortices give way to two large counter-rotating vortices and a small vortex breakdown underneath the impeller hub, a well-known phenomenon in the context of a rotating disk inside a closed cylindrical tank (i.e., a rotor-stator configuration (Daube, 1991; Kahouadji, 2011; Spohn, 1991; Spohn et al., 1998)). These vortical structures described for $f = 8$ Hz are also observed for the entire range

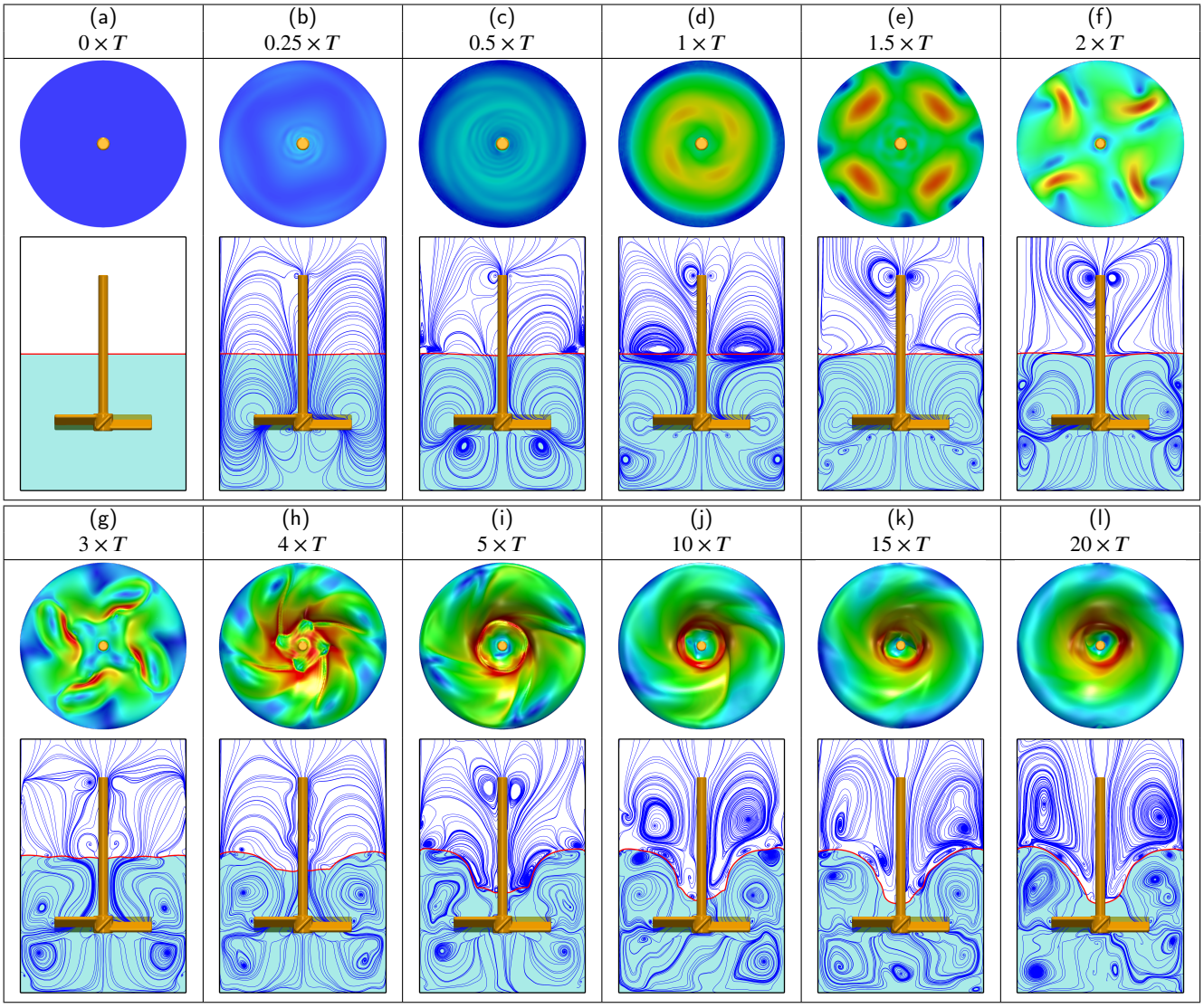

Figure 3: Spatio-Temporal evolution of the flow for water, vortical structures, and interface shapes coloured by velocity magnitude shown in the lower and upper figures in every panel, respectively, for a rotating frequency $f = 1/T = 8$ Hz. The dimensionless numbers are $Re \sim 6.28 \times 10^4$, $Fr \sim 3.22$, $We \sim 1.08 \times 10^3$. (see Supplementary Material "Animation-Fig3.avi")

of frequency $f \leq 9$ Hz as shown in Fig. 4 which shows the spatio-temporal evolution of the interface and vortical structures in a two-dimensional plane for $f = 5$, 7, and 9 Hz for $t = 0.25 \times T$-$15 \times T$ (see also the supplementary Material "Animation-Fig5.avi"). It is also clear upon inspection of Fig. 4 that there are strong qualitative similarities amongst the vortical structures for this range of frequencies (and, in turn, Re and We) for $t \leq 2 \times T$.

Figure 5-(a)-(f) depicts snapshots of the interface shape, and accompanying structures in the vorticity and pressure fields at $t/T = 20$ for $f = 5 - 9.5$ Hz. It is clear that the salient points highlighted for $f = 8$ Hz in Fig. 3 are observed for the entire frequency range. Figure 5-(g), shows the temporal evolution of the global kinetic energy of the flow, $\kappa = \left(\int\int\int \rho \mathbf{u}^2 dxdydz\right)$, and Fig. 5-(h) shows the variation of the minimum position of the interface with time for the range of frequency $f = 5$ to 9.5 Hz. For $f = 5$ Hz, the interface deflection is small compared to other cases and a vortex breakdown attached to the interface occurs; this phenomenon is also observed for rotating disks inside an open cavity (Kahouadji and Martin Witkowski, 2014; Piva and Meiburg, 2005; Spohn, 1991; Spohn et al., 1993, 1998). In certain cases, there is an appearance of a small vortex at the bottom corner of the vessel or at the top corner (see Fig. 5-(c) for $f = 7$ Hz). For $f = 9.5$ Hz, the interface just reaches the hub of the impeller (see Fig 5-(f)). For this set of parameters, this frequency represents the limit for efficient mixing without entraining bubbles into the water phase. At $t = 20 \times T$, we consider that the flow is in a quasi-steady state as the curves corresponding to Fig. 5-(g)-(h) flatten, particularly for the range $f = 5 - 8$ Hz. For $f = 9$ and 9.5 Hz, although the the kinetic energy appears to plateau for $t \geq 10 \times T$, the minimal interfacial position exhibits small-amplitude, high-frequency oscillations related to the

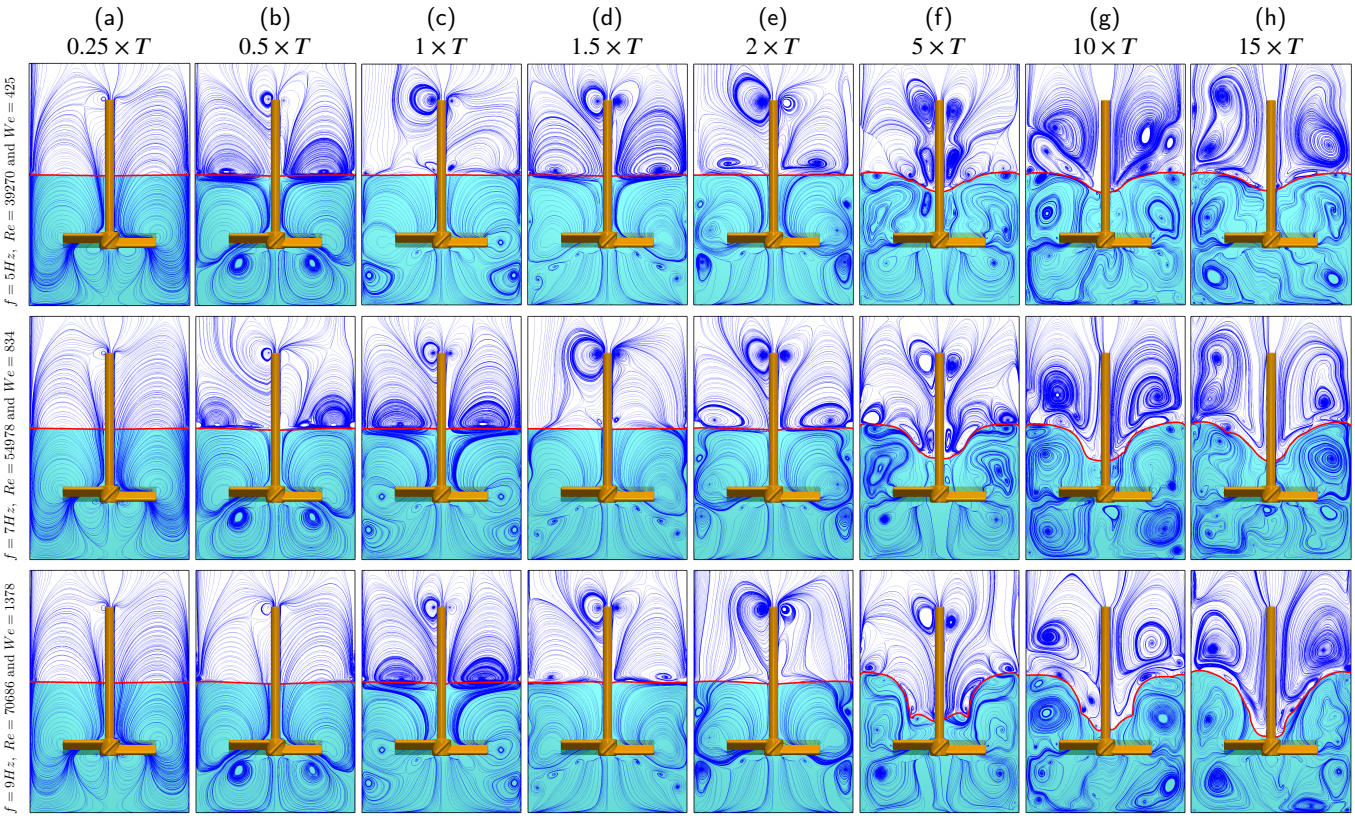

Figure 4: Spatio-temporal evolution of vortical structures for three different rotational frequencies, from top to bottom, $f = 1/T = 5$, 7 and 9 Hz, respectively, using the physical properties of water, for $t = 0.25 \times T$-$15 \times T$. The corresponding Reynolds and Weber number combinations are $(Re, We) = (39270, 425)$, $(54978, 834)$ and $(70686, 1378)$, respectively. (see Supplementary Material "Animation-Fig4.avi")

interaction of the interface with the impeller hub.

The pressure field shown in Fig. 5 for all values of f illustrates the dominance of the vortical structures on the pressure field. For small rotation frequency values ($f \leq 5Hz$), the behaviour of the pressure is hydrostatic, decreasing linearly as a function of z-direction. This type of pressure field distribution is observed for $f = 5$ Hz (see Fig. 5-(a)). Increasing the frequency up to 6 Hz, the pressure field still varies linearly through z-direction; however, a depression zone is noticed at the back of the blades (see pressure field in 5-(b-f)). This depression is a characteristic of flows past an obstacle, which means that in the rotating blades reference, the front and back of the blades are zones of high and low pressure, respectively. In addition to these low and high pressure zones near the blades, we can notice that for high values of rotation frequency ($f \geq 7$ Hz), the eddy structures break the hydrostatic form of the pressure field and a high pressure zone is localised only near the bottom outer edge of the vessel.

3.3. Transition to aeration

In this section, we will focus on the air-water system and elucidate mechanisms that lead to entrainment of air bubbles into the water phase via careful examination of the transition boundary between the vortex and bubbly mixing regimes. In order to perform accurate simulations of the onset of aeration, all simulations presented in this section are performed using $4 \times 4 \times 6 = 96$ subdomains, with a Cartesian structured grid of 64^3 per subdomain, which gives a global structured mesh of $256 \times 256 \times 384$.

Figure 6 depicts the interfacial dynamics associated with the $f = 10$ Hz case, characterised by $Re = 78540$ and $We = 1713$. The results presented thus far were generated by starting from an initially flat interface and a velocity field at rest ($\mathbf{u} = \mathbf{0}$). Using this initialisation, it is seen clearly that the interface, which interacts with the impeller hub, undergoes breakup leading to the formation of three small bubbles that are entrained into the water phase. If, however, the simulation is initialised starting from the steady-state associated with the $f = 8$ Hz case, but with $f = 10$ Hz, then we find that the outcome (not shown) corresponds to a vortex mixing regime, similar to that shown in Fig. 5-(f).

In order to elucidate the mechanisms underlying aeration, we focus on the case wherein the flow is started impulsively from an initially stationary flat-interface state. As a result of the impeller rotation, a low pressure region forms near the impeller hub that leads to a large interfacial deflection and the formation of a thin air ligament at the back of one of the blades; this is a consequence of the centrifugal

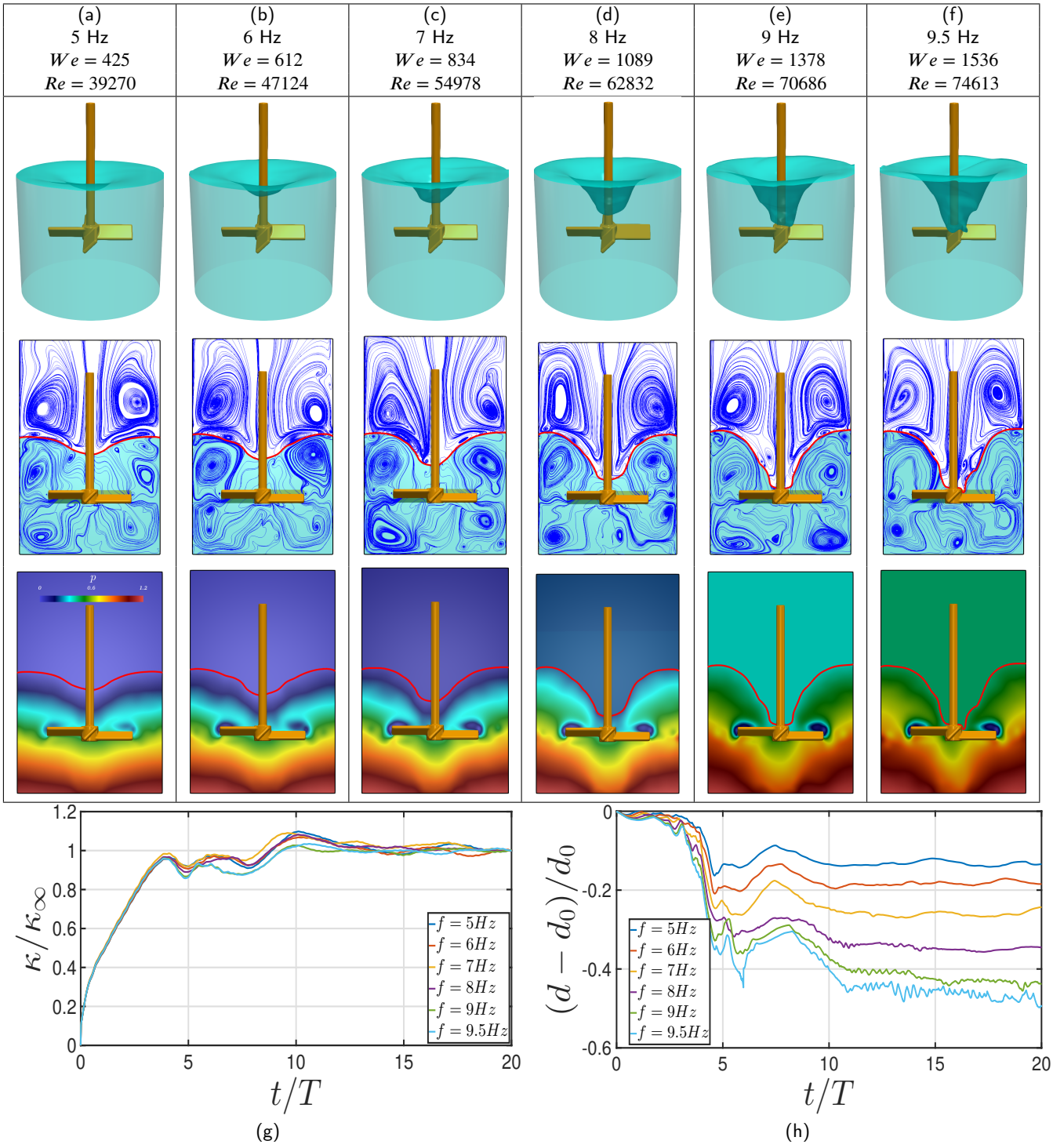

Figure 5: Interface shape, vortical structures, and pressure fields for the flow of water in a two-dimensional vertical plane at $t/T = 20$ for rotating frequency given from (a) to (f), $f = 5, 6, 7, 8, 9$ and 9.5 Hz, respectively. Panels (g) and (h) show the temporal evolution of the kinetic energy normalised by its terminal value, and the minimum interface position normalised by its initial value, respectively. (see Supplementary Material "Animation-Fig5.avi")

forces that drive ligament elongation in the radial direction away from the hub. The ligament eventually undergoes a Rayleigh-Plateau instability and breakups into three small bubbles (see Fig. 6 c, d, and e). Thus, the route to bubble creation, and subsequent aeration of the water phase, involves three successive mechanisms: (i) a sufficiently strong centrifugal force able to deform the interface rapidly toward the impeller hub; (ii) ligament formation that grows radially behind a blade; (iii) a Rayleigh-Plateau-driven breakup of the ligament. The example shown in Fig. 6 features the forma-

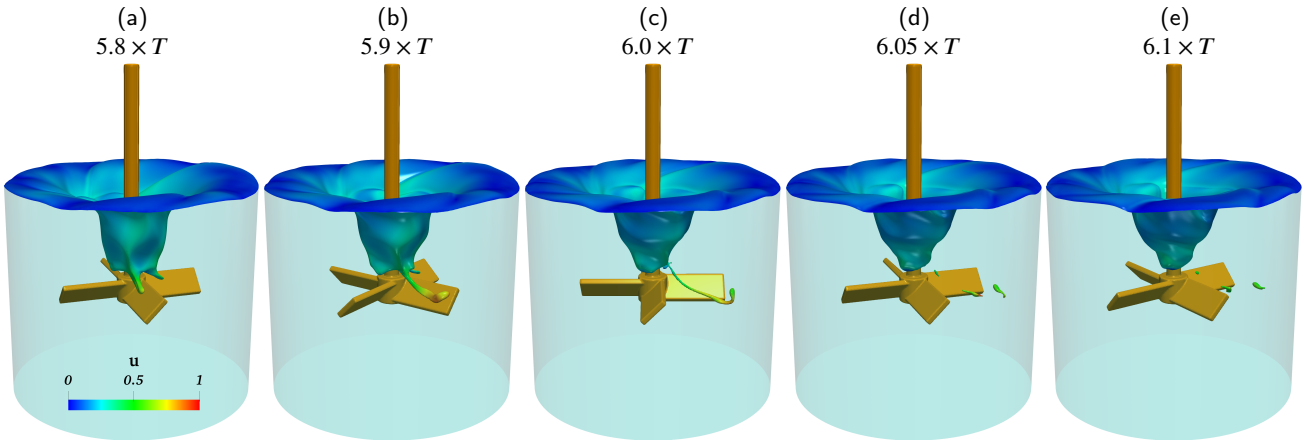

Figure 6: Spatio-temporal evolution of the mixing behaviour for $f = 1/T = 10$ Hz, $Re = 78540$, and $We = 1713$ highlighting the primary aeration process. (see Supplementary Material "Animation-Fig6.avi")

tion of only one air ligament and its breakup. We will show that further increase in rotating frequency causes simultaneous entrapment and growth of multiple ligaments, leading to a more violent transition into the bubbly mixing regime.

3.4. Bubbly mixing

After the brief discussion of the mechanisms underlying aeration mixing, we now increase the impeller rotation frequency to $f = 11$ Hz ($Re = 86394$ and $We = 2073$) for which the outcome is very bubbly with a total number of air bubbles being of the order of hundreds dispersed inside the water phase. Figure 7 shows the spatio-temporal evolution of the flow where it is seen that the initially flat interface experiences a rapid deflection (see Fig. 7 a, b, & c) toward the impeller blades (see Fig. 7 e-f) with some interfacial pinchoff without yet significant ligament formation and breaking (see Fig. 7 g-h).

At $t = 4.25 \times T$, four air ligaments are formed, which grow quickly in the radial direction, and breakup into many bubbles (see Fig. 7 i-j). The resulting air-ligaments forming behind each blade are not as thin as in the case described for $f = 10$ Hz (see Fig. 6). As highlighted through Fig. 7 j-k, thick shaped air ligaments will breakup and disperse all around the liquid water phase. This process continues and produces a myriad of multiscale air-bubbles. Some of these bubbles have the shape of elongated thin air ligaments, also dispersed in the water phase, and eventually breakup later into smaller bubbles.

The flow is also accompanied by a series of coalescence events that occur between bubbles inside the water phase as well as with the main top interface. Small bubbles usually remain in the water phase but larger bubbles, due to buoyancy, rise to the top. When any bubble reaches the main top interface, it bursts and sometimes ejects some liquid-droplets above the interface (Fig. 7 n-o).

In Fig. 8, we have isolated several 'singular' events that involve topological transitions occurring in this type of bubbly mixing. Figure 8a highlights a coalescence event between a small bubble and the main interface. These snapshots in Fig. 8a are given at the following times, from top to bottom, $t/T = 5.92$, 5.94, and 5.96, respectively. We can notice that the small bubble coalesces with the vertical part of the main interface that surrounds the impeller shaft. In Fig. 8b, we have also isolated the breakup event of a ligament. We can notice a rapid coalescence of a tiny bubble with this ligament before experiencing two interfacial breakups later.

Figure 8c shows the temporal evolution of a bubble bursting through the main top interface, generating liquid ligaments above this interface, and finally breaking up into a multitude of droplets that will fall back to the liquid bulk later on. Contrary to the coalescence described in Fig. 8a, when a bubble hits the top interface, it bursts. However, if a bubble hits the vertical part of the main interface, the outcome is described as a simple coalescence process. Furthermore, for the latest snapshot of Fig. 8c, we count a total of 503 bubbles dispersed inside the bulk of the water phase, and also a total 33 water drops. Some of the water drops are located above the main top interface (see the latest snapshots Fig. 8c), but some other liquid droplets are encapsulated inside some large bubbles inside the water bulk.

At this stage of the mixing process, it is interesting to follow the temporal evolution of these bubble sizes during the aeration process. We can notice through Fig. 7 that the appearance of bubbles in the liquid bulk starts at time $t/T \approx 4.5$ (see Fig. 7g). Moreover, the flow can be considered as 'bubbly' only at $t/T \approx 5.5$ (Fig. 7k). It is possible to isolate all n bubbles dispersed within the water phase, calculate the volume of each individual bubble $\mathcal{V}_{b,i}$ ($i = 1, n$), and deduce an approximation of its diameter $d_{b,i} = (6\mathcal{V}_{b,i}/\pi)^{(1/3)}$. Figure 9(a) represents the probability density function of bubble size distribution for $t/T = 5.5$, 6, and 6.5. It is during this time range $t/T = 5.5 - 6.5$ that the flow transitions from quasi-stratified to bubbly. The bubbles at $t/T = 5.5$ are relatively large compared to $t/T \geq 6$ due to the presence of four thick air-ligaments behind each blade that have not broken up

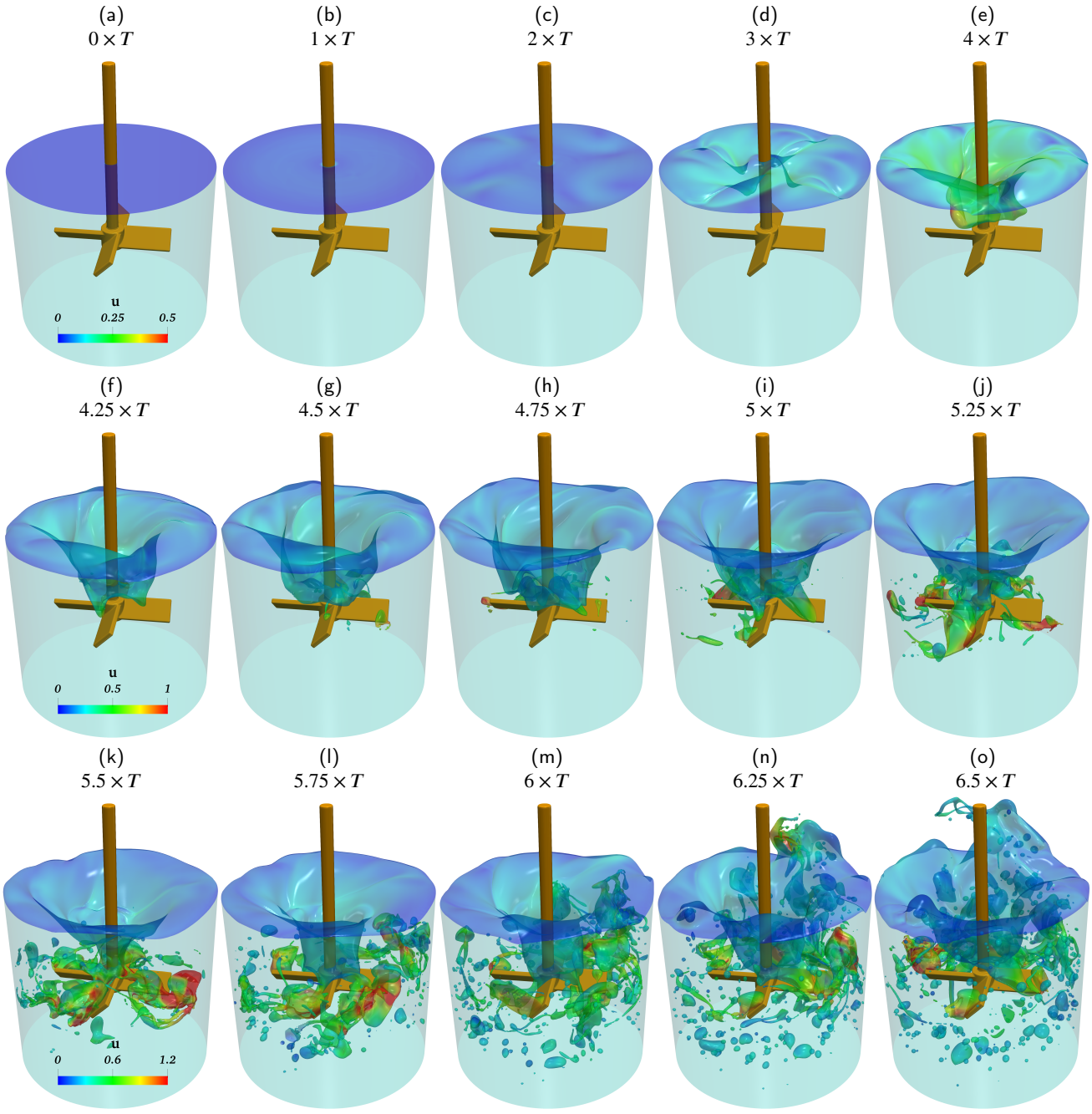

Figure 7: Spatio-temporal evolution for bubbly mixing with $f = 1/T = 11$ Hz, $Re = 86394$, and $We = 2073$. (see Supplementary Material "Animation-Fig7.avi")

entirely (see Fig. 7k). However, most of the bubble sizes are smaller than the average value d_{bm}. For $t/T \geq 8$, the probability density functions are nearly identical (see Fig. 9b). Even if there are still a multitude of singular events (e.g. bubble entrainment, coalescence, breakup, bursting) continuing to occur, the aeration process for $f = 11$ Hz can be considered as full-developed for $t/T \geq 8$.

Finally, from an engineering perspective, it is crucial to estimate the air bubble volume dispersed inside the water phase. As mentioned in the introduction, for some applications, bubbles can be desired and sometimes their appearance should be avoided. However, if these air bubbles are produced during a mixing process, it is important to estimate the temporal evolution of the gas holdup, ε:

$$\varepsilon(t) = \mathcal{V}_b / \left(\mathcal{V}_b + \mathcal{V}_l\right) \tag{11}$$

which is the ratio of the volume of the air phase entrained within the water, $\mathcal{V}_b = \sum_{i=1}^{n} \mathcal{V}_{b,i}$, to the total volume of air and water within the stirred vessel; $\mathcal{V}_l = \pi D_b^2 h/4$ is the

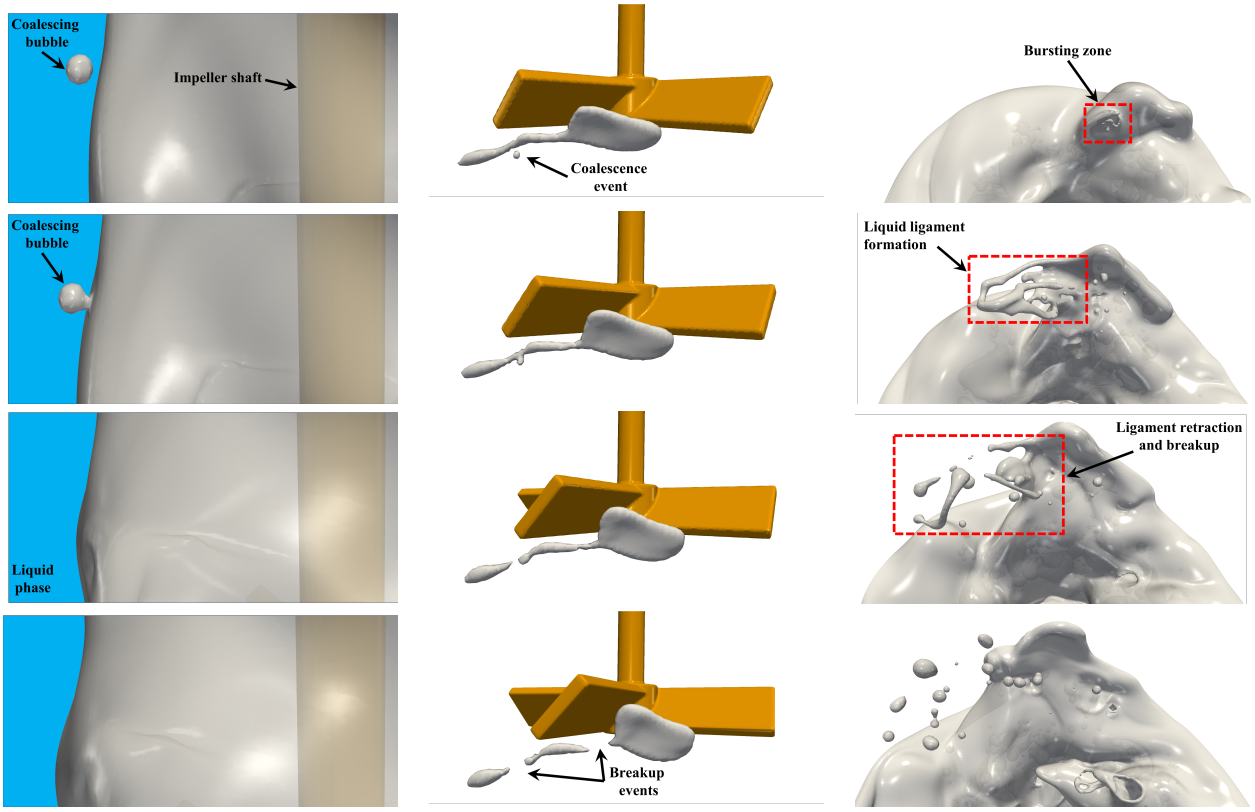

Figure 8: Flow snapshot for $f = 1/T = 11$ Hz, $Re = 86394$, and $We = 2073$ highlighting singularity mechanisms: (a) coalescence of a tiny bubble with the main interface, (b) ligament breakup events, and (c) bubble bursting through the main top interface.

volume of the water phase. In Fig. 9(c), we show the evolution of the gas holdup $\epsilon(t)$ highlighting its maximum value at $t/T \approx 6.25 - 6.5$ beyond which the dynamic equilibrium amongst bubble formation, coalescence, and breakup leads to a steady ϵ. Inspection of Fig. 9(c) reveals that this steady-state is reached for $t/T \geq 8$ with about 1.9% of air dispersed in the water bulk.

4. Conclusion and perspectives

In this paper, we study numerically the complex dynamics occurring during air-liquid mixing using a pitched blade turbine. The motion of the impeller and the fluid-structure interaction is computed by a direct forcing method within a general solver for multiphase flows (Shin et al., 2017). We have shown that vortical structures are similar for any frequency below the aeration limit. These vortical structures are Kelvin-Helmholtz, blade tip, end wall, and wall breakdown vortices. Aeration occurs for large rotational frequency, and we highlight the importance of the initial state (from rest or from a developed situation). Future research avenues for study are to investigate further the physics of the aeration (for frequency larger than 10 Hz), generalise this study through variation of the initial liquid height, the clearance and the diameter ratio between the impeller and the cylindrical tank. Another type of multiphase mixing process that has not been studied here and occurs for high frequencies $f \geq 15$ Hz, is 'air envelopment' mixing. At very high rotation frequencies, the air phase will envelop the entire impeller during the rotation. It would also be interesting to explore different types of impellers (e.g., Rushton turbines, propellers or curved blade turbines). Finally, in considering non-Newtonian fluids or the presence of surfactants, the recent paper of Shin et al. (2018) has moved the numerical method in those directions and thus these effects could, in the future, be modelled too.

Acknowledgements

This work is supported by the Engineering & Physical Sciences Research Council, United Kingdom, through the MEMPHIS (EP/K003976/1) and PREMIERE (EP/T000414/1) Programme Grants, and by computing time at HPC facilities provided by the Research Computing Service (RCS) of Imperial College London. DJ and JC acknowledge support through computing time at the Institut du Developpement et des Ressources en Informatique Scientifique (IDRIS) of the Centre National de la Recherche Scientifique (CNRS), coordinated by GENCI (Grand Equipement National de Calcul Intensif) Grant 2020 A0082B06721. LK acknowledges with gratitude P. Dossin, H. Hu and Z. Alam for the warm hospitality at Procter & Gamble where this study has been initiated. Simulations have been performed using code BLUE (Shin et al., 2017) and the visualisations have been generated using Paraview.

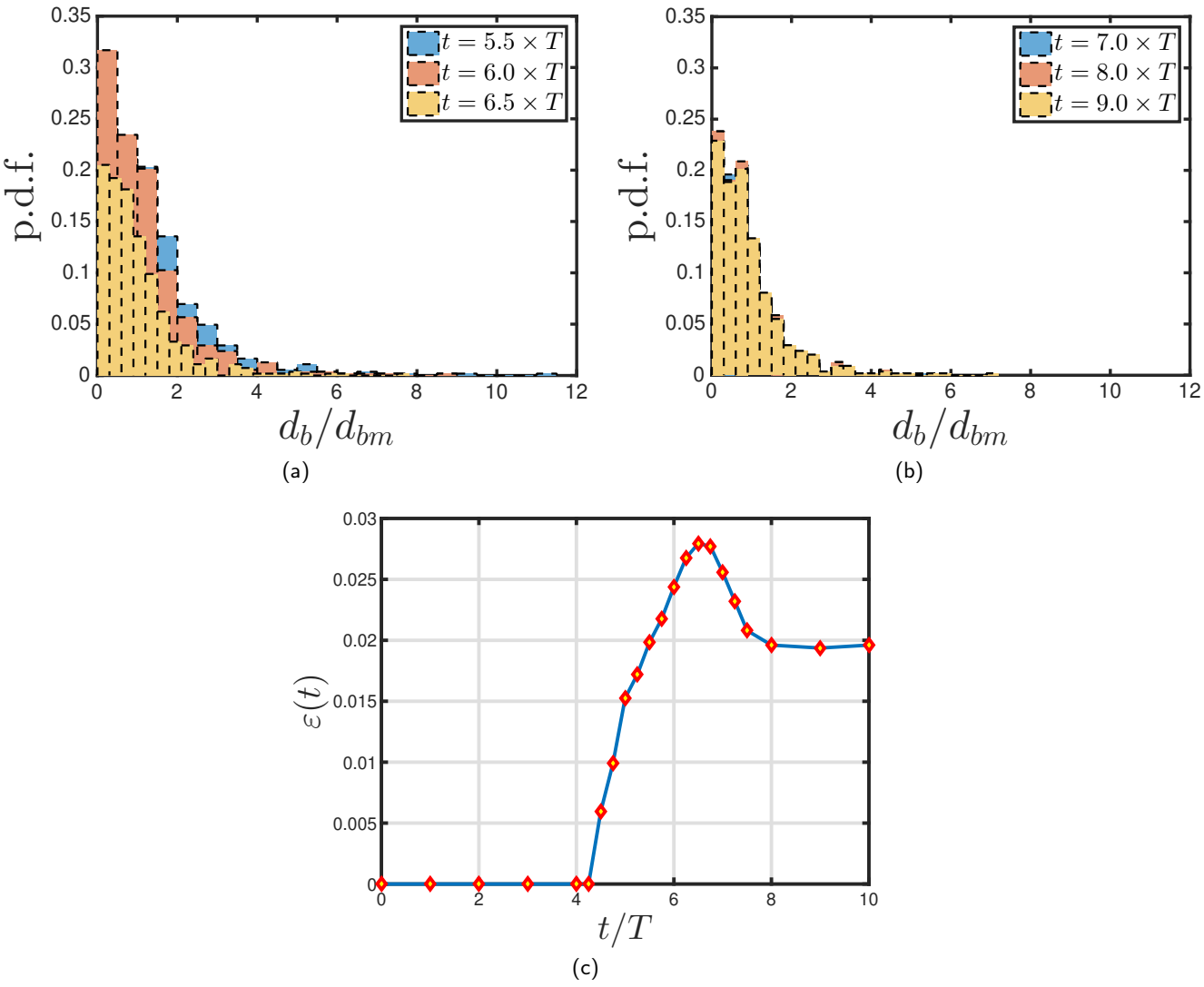

Figure 9: Probability density function histogram of bubble size inside the liquid bulk, normalised by the average bubble diameter, d_{bm}, associated with the times (a): t/T = 5.5, 6, 6.5, and (b): t/T = 7, 8, 9, respectively. (c): temporal evolution of the gas holdup $\varepsilon(t)$. The rest of the parameter values are the same as those used to generate Fig. 7.

References

Batels, C., Breuer, M., Wechdler, K., Durst, F., 2002. Computational fluid dynamics applications on parallel-vector computer: computations of stirred vessel flows. Comp. Fluids 31, 69–97.

Brucato, A., Ciofalo, M., Grisafi, F., Micale, G., 1998. Numerical prediction of flow fields in baffled stirred vessels: A comparison of alternative modelling approaches. Chem. Eng. Sci. 53, 3653–3684.

Ciofalo, M., A. Brucato, A., Grisafi, F., Torraca, N., 1996. Turbulent flow in closed and free-surface unbaffled tanks stirred by radial impellers. Chem. Eng. Sci. 51, 3557–3573.

Daube, O., 1991. Numerical simulation of axisymmetric vortex breakdown in a closed cylinder. American Math. Soc. 28.

Fadlun, E.A., Verzicco, R., Orlandi, P., Mohd-Yusof, J., 2000. Combined immersed-boundary finite-difference methods for three-dimensional complex flow simulations. J. Comp. Phys. 161, 35–60.

Harlow, F.H., Welch, J.E., 1965. Numerical calculation of time dependent viscous incompressible flow of fluid with free surface. Phys. Fluids 8, 2182–2189.

Jansson, T.R.N., Haspang, M.P., Jesen, K.H., Hersen, P., Bohr, T., 2006. Polygons on a rotating fluid surface. Phys. Rev. Lett. 96, 174502.

Kahouadji, L., 2011. Linear stability analysis for free surface rotating flow. Ph.D. thesis. Université Pierre & Marie Curie - Paris VI.

Kahouadji, L., Martin Witkowski, L., 2014. Free surface due to a flow driven by a rotating disk inside a cylindrical tank: Axisymmetric configuration. Phys. Fluids 26, 072105.

Kahouadji, L., Nowak, E., Kovalchuk, N., Chergui, J., Juric, D., Shin, S., Simmins, M.J.H., Craster, R.V., Matar, O., 2018. Simulation of immiscible liquid-liquid flows in complex micro-channel geometries using a front-tracking scheme. Microfluidics and Nanofluidics 22, 126.

Kwak, D.Y., Lee, J.S., 2004. Multigrid algorithm for the cell-centred finite difference method ii: Discontinuous coefficient case. Wiley InterScience (www.interscience. com) .

Launder, B.E., Spalding, D.B., 1974. The numerical computation of turbulent flows. Comp. Meth. Appl. Mech. Engineering 3, 260–289.

Li, L., Wang, J., Feng, L., Gu, X., 2017. Computational fluid dynamics simulation of hydrodynamics in an uncovered unbaffled tank agitated by pitched blade turbines. Korean J. Chem. Eng. 34, 2811–2822.

Lopez, J.M., 1995. Unsteady swirling flow in an enclosed cylinder with reflectional symmetry. Phys. Fluids 7, 2700–2714.

Mohd-Yusof, J., 1997. Combined immersed-boundary / b-spline methods for simulations of flow in complex geometries. Center for Turbulence

Research Annual Research Briefs , 317–327.
Peskin, C.S., 1977. Numerical analysis of blood flow in the heart. J. Comp. Phys. 25, 220–252.
Piva, M., Meiburg, E., 2005. Steady axisymmetric flow in an open cylindrical container with a partially rotating bottom wall. Phys. Fluids 17, 063603.
Poncet, S., 2005. Écoulements de type rotor-stator soumis à un flux axial: de Batchelor à Stewartson. Ph.D. thesis. Université de Provence Aix-Marseille I.
Saad, Y., 2003. Iterative Methods for Sparse Linear Systems. 2^{nd} Edition, Society for Industrial and Applied Mathematics.
Shin, S., 2007. Computation of the curvature field in numerical simulation of multiphase flow. J. Comp. Phys. 222, 872–878.
Shin, S., Juric, D., 2009. A hybrid interface method for three-dimensional multiphase flows based on front tracking and level set techniques. Int. J. Numer. Meth. Fluids 60, 753–778.
Shin, S., Chergui, J., Juric, D., 2017. A solver for massively parallel direct numerical simulation of three-dimensional multiphase flows. J. Mech. Sci. Tech. 31, 1739.
Shin, S., Chergui, J., Juric, D., Kahouadji, L., Matar, O., Craster, R.V., 2018. A hybrid interface tracking - level set technique for multiphase flow with soluble surfactant. J. Comp. Phys. 359, 409–435.
Spohn, A., 1991. Ecoulement et éclatement tourbillonnaire engendré par un disque tournant dans une enceinte cylindrique. Ph.D. thesis. Université de Grenoble I.
Spohn, A., Mory, M., Hopfinger, E., 1993. Observations of vortex breakdown in an open cylindrical container with a rotating bottom. Exp. Fluids 14, 70–77.
Spohn, A., Mory, M., Hopfinger, E., 1998. Experiments on vortex breakdown in a confined flow generated by a rotating disc. J. Fluid Mech. 370, 73–99.
Stewartson, K., 1953. On the flow between two rotating coaxial disks. Proc. Camb. Phil. Soc. 49, 9 :333–341.
Suzuki, T., Iima, M., Hayase, Y., 2006. Surface switching of rotating fluid in a cylinder. Phys. Fluids 18, 101701.
Vatistas, G.H., 1990. A note on liquid vortex sloshing and kelvin's equilibria. J. Fluid Mech. 217, 41–248.
Vatistas, G.H., Wang, J., Lin, S., 1992. Experiments on waves induced in the hollow core vortices. Exp. Fluids 13, 377–385.